The Astrophysical Journal Letters, 816:L9 (6pp), 2016 January 1 doi:10.3847/2041-8205/816/1/L9

HYDRODYNAMIC MOVING-MESH SIMULATIONS OF THE COMMON ENVELOPE PHASE IN BINARY STELLAR SYSTEMS

Sebastian T. Ohlmann[1,2], Friedrich K. Röpke[1,3], Rüdiger Pakmor[1], and Volker Springel[1,4]
[1] Heidelberger Institut für Theoretische Studien, Schloss-Wolfsbrunnenweg 35, D-69118 Heidelberg, Germany
[2] Institut für Theoretische Physik und Astrophysik, Universität Würzburg, Emil-Fischer-Str. 31, D-97074 Würzburg, Germany
[3] Zentrum für Astronomie der Universität Heidelberg, Institut für Theoretische Astrophysik, Philosophenweg 12, D-69120 Heidelberg, Germany
[4] Zentrum für Astronomie der Universität Heidelberg, Astronomisches Recheninstitut, Mönchhofstr. 12-14, D-69120 Heidelberg, Germany
Received 2015 October 13; accepted 2015 December 11; published 2015 December 30

ABSTRACT

The common envelope (CE) phase is an important stage in binary stellar evolution. It is needed to explain many close binary stellar systems, such as cataclysmic variables, SN Ia progenitors, or X-ray binaries. To form the resulting close binary, the initial orbit has to shrink, thereby transferring energy to the primary giant's envelope that is hence ejected. The details of this interaction, however, are still not understood. Here, we present new hydrodynamic simulations of the dynamical spiral-in forming a CE system. We apply the moving-mesh code AREPO to follow the interaction of a $1M_{\odot}$ compact star with a $2M_{\odot}$ red giant possessing a $0.4M_{\odot}$ core. The nearly Lagrangian scheme combines advantages of smoothed particle hydrodynamics and traditional grid-based hydrodynamic codes and allows us to capture also small flow features at high spatial resolution. Our simulations reproduce the initial transfer of energy and angular momentum from the binary core to the envelope by spiral shocks seen in previous studies, but after about 20 orbits a new phenomenon is observed. Large-scale flow instabilities are triggered by shear flows between adjacent shock layers. These indicate the onset of turbulent convection in the CE, thus altering the transport of energy on longer timescales. At the end of our simulation, only 8% of the envelope mass is ejected. The failure to unbind the envelope completely may be caused by processes on thermal timescales or unresolved microphysics.

Key words: binaries: close – hydrodynamics – methods: numerical – stars: kinematics and dynamics

1. INTRODUCTION

Many relevant astrophysical processes involve a compact star in a close binary system, e.g., cataclysmic variables, SN Ia progenitors, X-ray binaries, or neutron star mergers. In the evolution of these systems, a giant in a wide orbit ejects its envelope while the orbit shrinks due to interaction with the binary companion in a common envelope (CE) event. Unstable mass transfer initiates a CE phase, followed by a rapid spiral-in and possibly further evolution on thermal timescales (for a recent review, see Ivanova et al. 2013). The first ideas were developed by Paczynski (1976), but the problem is still far from being understood today. Hence, binary population synthesis codes model CE phases using parametrized prescriptions where the uncertainty of the outcome is dominated by the parametrization of these phases (compare, e.g., the study by Meng et al. 2011 for SN Ia progenitors). As the CE phase does not possess intrinsic symmetries, hydrodynamical simulations in three dimensions are required to model the physical processes. Some processes may take place on a thermal timescale where hydrodynamic simulations are not feasible today and should be complemented by one-dimensional simulations including more physics, e.g., energy transport (see the discussion in Ivanova et al. 2013).

Recent hydrodynamic simulations include the adaptive mesh refinement (AMR) simulations by Ricker & Taam (2008, 2012) and the smoothed particle hydrodynamics (SPH) and unigrid simulations by Passy et al. (2012). In these calculations, the dynamical spiral-in lasts between 10 and 100 days, during which spiral shocks redistribute angular momentum in the envelope. At the end, only a small fraction of the envelope becomes unbound and the final separation seems to be larger than in observed post-CE systems (compare Figure 17 of Passy et al. 2012). The failure to eject the envelope in current simulations may possibly be overcome by including recombination energy (see SPH simulations by Nandez et al. 2015).

To improve the understanding of hydrodynamical processes during the spiral-in phase of a CE event, we have run a high-resolution simulation using the moving-mesh code AREPO (Springel 2010). This code solves the Euler equations on a moving computational grid with adaptive resolution, thus combining the advantages of traditional SPH and AMR codes, e.g., conservation of angular momentum and total energy and resolution of low-mass flows and small-scale flow features. Here, we show that the AREPO code, developed originally for cosmological simulations (e.g., Marinacci et al. 2014; Vogelsberger et al. 2014), allows us to resolve the hydrodynamical structure of the CE phase in unprecedented detail. In our simulation, shear flows lead to large-scale Kelvin–Helmholtz instabilities that dominate the flow structure. These instabilities have not been observed previously in simulations and may mark the onset of convection, thus changing the transport of energy in the envelope on a thermal timescale.

2. NUMERICAL METHODS AND SETUP

We simulate the dynamical spiral-in of the CE phase with the finite volume hydrodynamics code AREPO (Springel 2010). AREPO solves the Euler equations on a moving, unstructured Voronoi mesh using an HLLC-type approximate Riemann solver. Self-gravity is included with a tree-based algorithm. We employ an improved gradient estimate and time integration scheme (Pakmor et al. 2016) yielding second order convergence also for general mesh motions. Individual and adaptive time stepping is used, which boosts the computational efficiency due to the multi-scale nature of the system: not all

cells are evolved on the shortest time step, but only the cells requiring the smallest time steps. Periodic boundary conditions were chosen for the hydrodynamics solver with the box size large enough (3.3×10^{14} cm), such that no mass flows over the boundary for a sufficiently long time. The simulation was stopped when the first outflow reaches the boundary.

The binary system was set up by placing a red giant (RG) model on the grid with the core replaced by a gravitation-only particle and then adding another gravitation-only particle to model a non-resolved, compact companion star, e.g., a main sequence star or a white dwarf. Thus, the simulation consists of cells representing the gas of the envelope and the background ("gas cells") and gravitation-only particles representing the RG core and the companion ("core cells").

For preparing the single-star initial conditions, we followed S. T. Ohlmann et al. (2016, in preparation). The RG model was created using the stellar evolution code MESA (Paxton et al. 2011, 2013) with a zero-age main sequence mass of $2M_\odot$. To limit the range in timescales, we replaced the core of the RG by a particle interacting only gravitationally. We mapped the resulting model to a grid with mass-adaptive radial shells using a HEALPix distribution (Górski et al. 2005) on each shell. The gravitational force of the particle was smoothed at a length of $h = 7.3 \times 10^{10}$ cm ($\sim 1.0 R_\odot$) according to the spline function given in Springel (2010). This enables us to reach a stable configuration around the particle since the pressure gradients can be resolved sufficiently to counteract the gravitational force of the particle. We treat the gas as an ideal gas with an adiabatic index of $5/3$ which is different from the MESA equation of state. However, since we are interested in the envelope where the departure from ideal gas behavior is small, this approach still allows for a reasonable representation of the star calculated with MESA in AREPO. The mechanical structure of the star is well reproduced in the envelope (differences in density, pressure, and sound speed are less than 5%). Only in the internal energy we observe larger deviations, because we neglect the ionization state of the gas as a first approximation. The RG atmosphere was then relaxed by employing an additional damping term to reduce spurious velocities for several dynamical timescales (for details, see S. T. Ohlmann et al. 2016, in preparation). This resulted in a stable profile with a core mass of $0.38M_\odot$ and an envelope mass of $1.60M_\odot$ (total: $1.98M_\odot$). The Mach numbers in the envelope reach up to 0.1 after the relaxation procedure, similar to what would be expected from the initial MESA model, although we are not able to properly resolve the convection in the envelope. The density and pressure profiles are stable for several dynamical timescales after relaxation without applying any damping. The total number of cells was about 1.8×10^6 with a mean cell mass of $8.7 \times 10^{-7} M_\odot$ at the beginning and 2.7×10^6 with $5.8 \times 10^{-7} M_\odot$ at the end of the simulation due to mesh refinement. The refinement criterion was set to a target cell mass of $8.4 \times 10^{-7} M_\odot$. Additionally, in a sphere of five softening lengths of the gravitation-only particle, the maximum cell radius was bound to a tenth of the softening length. The smallest cells near the RG core have a radius of about 4.6×10^9 cm ($0.07 R_\odot$) at the beginning and about 8×10^8 cm ($0.01 R_\odot$) at the end of the simulation. This allows us to study small-scale flow features in detail. In the direct vicinity of the RG core, the hydrodynamical flow is only resolved outside of a sphere of radius of the softening length. Nevertheless, we find that a resolution of about 10 cells per

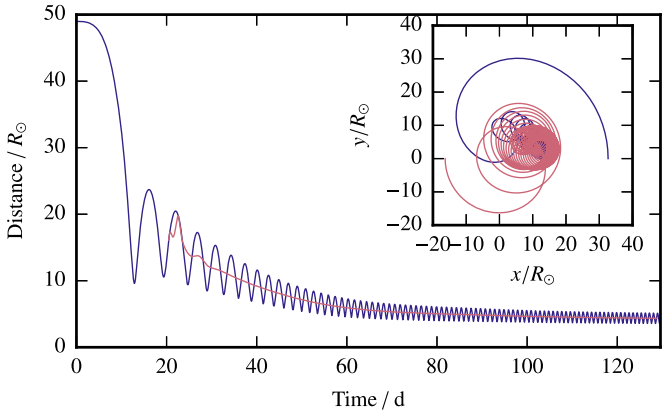

Figure 1. Distance of RG core and companion (blue) and major semi-axis (red) in solar radii over time in days. The inset shows the positions of the RG core (red) and companion (blue) in the x–y plane up to 80 days.

softening length is required to ensure energy conservation during the in-spiral. The spatial resolution in recent hydrodynamics simulations of CE phases was lower: the AMR simulations of Ricker & Taam (2008, 2012) have $0.3 R_\odot$ cells for a $32 R_\odot$ RG, the SPH simulations of Passy et al. (2012) have $0.1 R_\odot$ smoothing lengths, and the grid simulations of Passy et al. (2012) $1.7 R_\odot$ and $3.4 R_\odot$ cells for a $83 R_\odot$ RG.

The companion was placed on the surface of the RG at the same y and z coordinates as the RG core and at a distance of $49 R_\odot$ in the x direction. The mass of the secondary was chosen to be $0.99 M_\odot$, half of the primary mass. The velocities were initialized to a rigid rotation around the center of mass with the Keplerian rotation period of 23 days. Moreover, the envelope was assumed to be in 95% co-rotation, similar to the simulations of Ricker & Taam (2008, 2012). More realistic initial conditions would start at the point of Roche lobe overflow to take into account the transfer of energy and angular momentum from the orbit to the envelope. Moreover, the hydrostatic equilibrium in the outer layers is less distorted compared to placing the companion at the surface. However, since the timescales of orbital decay are very long when the first mass transfer starts, it is at the moment computationally infeasible for us to start the simulation at the Roche lobe distance.

The RG atmosphere and the companion were placed in a large box with a side length of 3.3×10^{14} cm and a low background density[5] of 10^{-16} g cm^{-3}. To resolve the gravitational interaction between the cores, the softening lengths of the cores are required to be at most a fifth of the distance between the cores. The simulation was stopped after about 120 days, when the first low-density tidal arm reached the boundary. Since the box was chosen very large, no mass is lost during the simulation. Angular momentum was conserved to high accuracy during the run with an error below 1%.

3. RESULTS AND DISCUSSION

The simulation starts with tidal deformation of the envelope and mass accretion on the secondary. When the accretion stream hits itself, shocks emerge and the orbit shrinks rapidly by a factor of five during the first revolution (Figure 1). This fast spiral-in slows down after a few orbits and the separation

[5] The density to which we resolve the initial RG model is 0.002 g cm^{-3}.

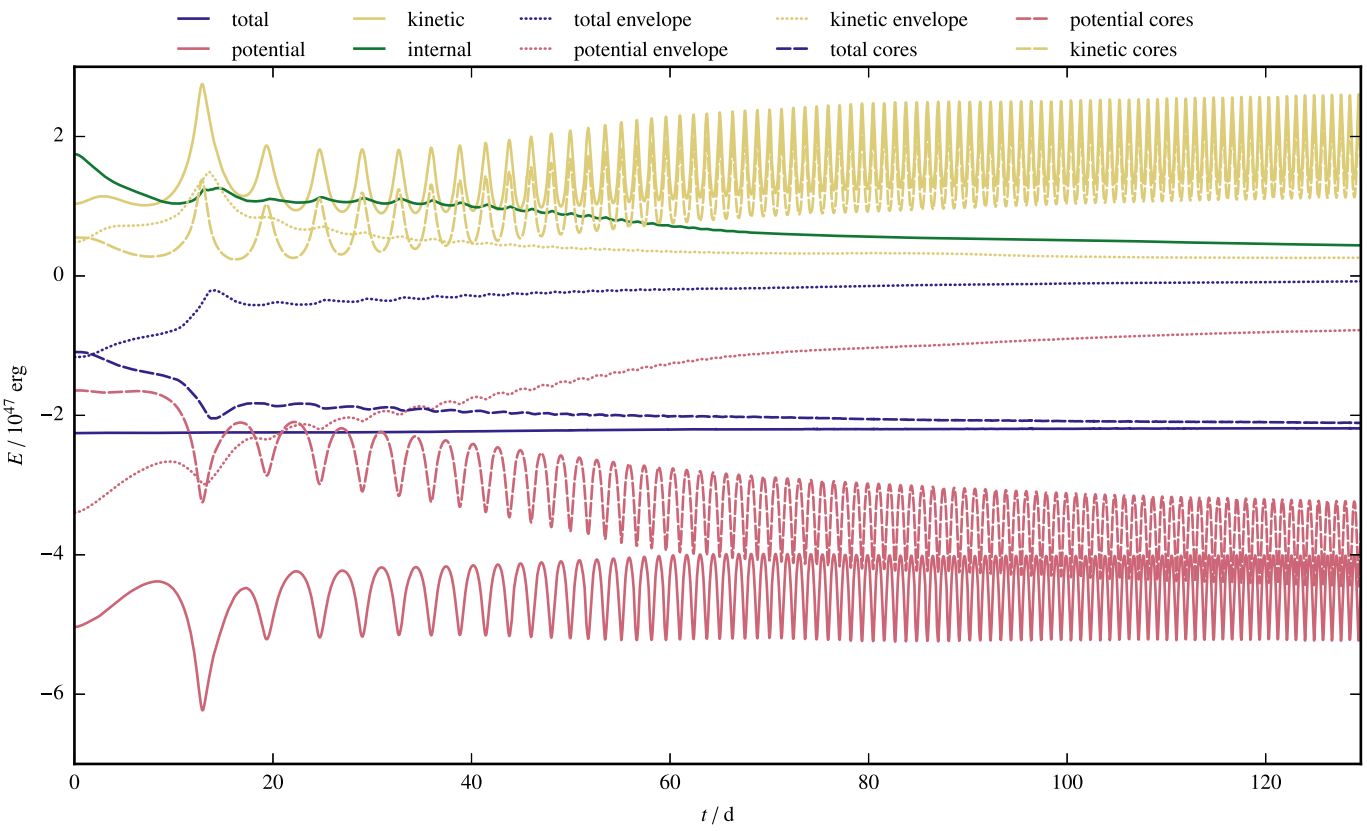

Figure 2. Energy budget during inspiral. Shown are the total (blue), potential (red), kinetic (yellow), and internal energy (green) for the gas of the envelope (dotted), the RG core and the companion (dashed), and summed values (full lines). The summed value of the internal energy is the same as for the gas since the RG core and the companion are gravitation-only particles. The conservation of the total energy is better than 3% during the simulation.

of the RG core and the companion decreases much slower at the end of the simulation. At this point, the system evolved for over 80 orbits and the separation is about $4.3R_\odot$, a factor of 10 smaller than in the beginning. The initially circular orbit becomes eccentric ($e \approx 0.5$), circularizes somewhat in the course of the spiral-in, and the eccentricity settles at a value of 0.18. Thus, the orbit is rather eccentric compared to the simulation by Ricker & Taam (2012) with $e = 0.08$ which may be due to different initial conditions. At the end of the simulation, the timescale of orbital decay ($-a/\dot{a}$, a: semimajor axis) grows to ∼1.5 years.

The energy budget during the simulation is shown in Figure 2 for the gas cells, the RG core and its companion, and the sum of both. In our simulation, the core cells interact only gravitationally, hence, they do not possess internal energy; thus the total internal energy is given by the gas of the RG envelope only. Although large amounts of potential and kinetic energy are converted into one another (up to 1.5×10^{47} erg in one orbit, i.e., 65% of the total energy), the total energy is conserved to better than 3% during the whole run. This means that our resolution is sufficient to accurately represent the regions where gravity is coupled strongly to the hydrodynamics and where the conversion between potential and kinetic energies takes place.[6]

During the simulation, energy is transferred from the binary system of the RG core and the companion to the envelope: its binding energy is raised from -1.2×10^{47} erg in the beginning to -7.7×10^{45} erg in the end of the simulation. This energy is mainly taken from the potential energy of the binary system of the RG core and the companion due to the shrinking orbit. The internal energy of the envelope decreases by 1.3×10^{47} erg because of its expansion. Although the total energy of the envelope is negative at the end of the simulation, $0.1M_\odot$ of the envelope gets unbound, about 8% of its mass. Most of this material is expelled during the first 40 days. After this, the mass loss rate settles to about $0.015M_\odot$ yr^{-1}. If this mass loss rate is sustained, the envelope may be ejected in roughly 100 years. Similar to the simulations by Passy et al. (2012) and Ricker & Taam (2008, 2012), only a small fraction of the envelope is unbound during the fast spiral-in, although more mass is lost in their simulations at a higher rate.

Since systems similar to the final system of our simulation are observed (e.g., J0755+4800 from Gianninas et al. 2014; a $\sim 0.4M_\odot + \sim 1M_\odot$ system in a $\sim 3R_\odot$ orbit), but in a shorter orbit and with the envelope ejected, additional mechanisms must contribute to the evolution that we do not capture in our simulation. This can either be processes acting on longer timescales (up to the thermal timescale) or additional micro-physical effects, such as recombination (compare the SPH simulations by Nandez et al. 2015).

The dynamics of the spiral-in is illustrated in Figure 3 as a series of density slices in the x–y plane. During the first orbit, the companion plunges into the envelope and an accretion stream onto it builds up. After 10 days (Figure 3, top left), an accretion shock is visible that results in a tidal arm moving outwards. Most of the material that is unbound at the end of the

[6] This is not trivial: due to the different discretization of gravity and hydrodynamics, problems with large conversions of potential energy into kinetic or internal energy can lead to substantial errors in the total energy, when the resolution is too low (see the Evrard collapse example in Springel 2010).

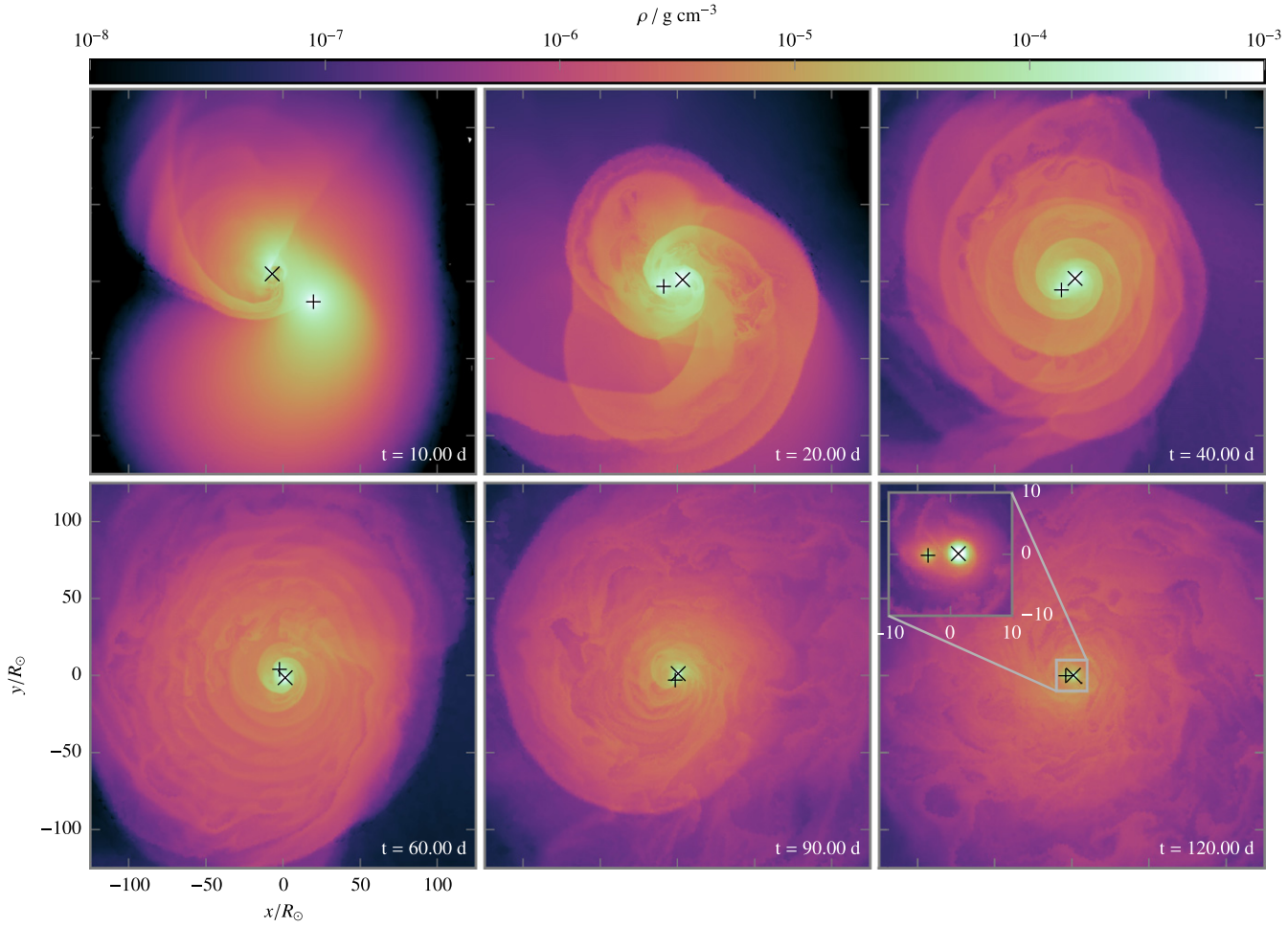

Figure 3. Time series of density snapshots in the x–y plane during spiral-in at six different times. The $\times$ marks the position of the companion, the $+$ marks the position of the RG core. All plots are centered on the center of mass of the RG core and the companion. The inset in the bottom right panel shows the central region of about $20R_\odot$ with the color scale ranging from 10^{-6} to 10^{-3} g cm^{-3}.

simulation stems from this first interaction. During the second orbit, the distance between the RG core and the companion has decreased by a factor of about 5 compared to their initial separation and the two compact components revolve in an eccentric orbit. The shock created by the companion reaches the inner part of the envelope while a second shock is caused by the motion of the RG core. After about two orbits (20 days, Figure 3, top middle), the shock created by the RG core overtakes the first tidal arm caused by the companion. The density field in the regions between the shocks does not show distinct features. After almost seven orbits (40 days, Figure 3, top right), a layered structure emerges that is created by spiral shocks continuously driven outwards by both the RG core and the compact companion. Shear flows between neighboring shocks cause Kelvin–Helmholtz instabilities in the outer part of the spiral structure. The spiral structure of the shocks tightens and shear instabilities grow stronger at 60 days (Figure 3, bottom left). At later times (90 days, Figure 3, bottom middle), shear instabilities of adjacent layers overlap and form a large-scale instability that connects several regions of the spiral structure. New shocks are still created in the inner part by the RG core and the companion. Near the end of the simulation (120 days, Figure 3, bottom right), the spiral shock structure is not visible anymore. Instead, large-scale instabilities have emerged and dominate the flow pattern. The central part of the domain around the compact components is still well resolved (see inset of the bottom right panel of Figure 3). The flow between the RG core and the companion remains smooth; shocks begin outside the innermost region. During the evolution, the flow shows some asymmetries caused by the first tidal arm which is ejected in the negative x and y directions, resulting in a relocation of the RG core and the companion in the opposite direction.

The structure of the envelope at the end of the simulation after 120 days is shown in Figure 4. The density slice in the x–y plane (Figure 4, top left) shows that the layered shock structure is only retained in the innermost region. In the outer region, it is washed out and the flow is dominated by large-scale instabilities. In the x–z plane (see middle left in Figure 4), the outflow is concentrated mostly around the equatorial plane in a toroidal structure. Shocks generated in the inner part are washed out by the shear instability in the outer region. To assess the convective stability of the envelope, we employ the Solberg–Høiland criterion (e.g., Kippenhahn et al. 2013) that predicts convective stability for

$$-\frac{\boldsymbol{g}\cdot\nabla s}{c_p}+\frac{1}{\varpi^3}\frac{\partial j^2}{\partial \varpi}>0, \tag{1}$$

where $\boldsymbol{g}$ denotes gravitational acceleration, s entropy, c_p specific heat capacity at constant pressure, j specific angular

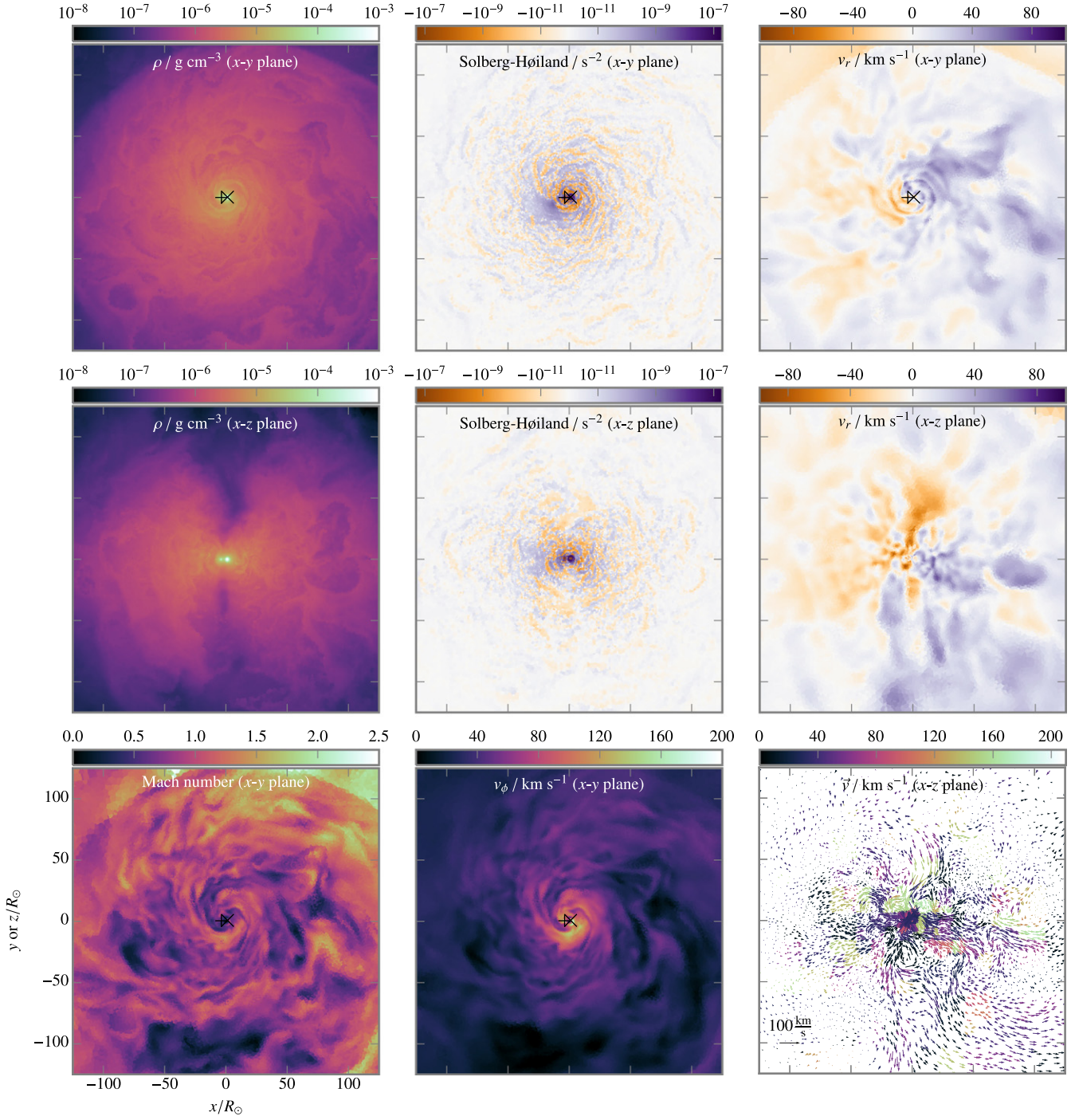

Figure 4. Late snapshot at 120 days. Shown are the density ρ in the x–y (top left) and x–z plane (middle left), the Solberg–Høiland criterion from Equation (1) using a symmetric logarithmic color coding (blue: stable; orange: unstable) in the x–y (top middle) and x–z plane (middle center), the radial component of the velocity $v_r = \boldsymbol{v} \cdot \boldsymbol{e}_r$ in the x–y (top right) and x–z plane (middle right), the Mach number (bottom left), the angular component of the velocity $v_\phi = \boldsymbol{v} \cdot \boldsymbol{e}_\phi$ (bottom middle), and a vector plot of the velocity in the x–z plane (bottom right), with the color coding indicating the magnitude of the velocity in km s^{-1}. The $\times$ marks the position of the companion, the $+$ marks the position of the RG core. All plots are centered on the center of mass of the RG core and the companion.

momentum, and ϖ distance from rotational axis. This quantity is shown in Figure 4 for the x–y plane (top middle) and the x–z plane (middle center). The flow is stabilized by the increase of specific angular momentum (second term) in a sphere of $\sim 7 R_\odot$ around the center of mass that is located to the lower left compared to the cores in Figure 4 (top middle). Farther away from the center of mass, the specific angular momentum is nearly constant, and the impact of the second term in the Solberg–Høiland criterion decreases rapidly. Apart from a small region of stability ($\sim 3 R_\odot$) around the RG core and the companion, regions of stability and instability alternate over the envelope because of the hydrodynamical flows. The situation is similar perpendicular to the orbital plane, where unstable regions can be found throughout the toroidal structure. The growth timescale associated to the unstable regions is $\lesssim$100 days; thus, we conclude that large parts of the envelope

should be convectively unstable. The radial velocity in the orbital plane (Figure 4, top right) displays some regions with inflows in the left hemisphere but outflows in the rest of the envelope. The inflow is probably caused by the initial plunge-in of the companion. The layered structure of the shocks is visible in the inner part as jumps, but it is overlaid by the instability farther out. In the x–z plane the radial velocity (Figure 4, middle right) shows mostly inflows in the upper and left hemispheres and outflows in the lower and right hemispheres. This pattern is also seen in the vector plot of the velocity in this plane (Figure 4, bottom right) that additionally shows a complex flow structure with whirls corresponding to the instabilities in the flow. This complex structure makes it difficult to predict the further evolution of energy transport in this plane. In the region of the developing instability, the flow is mostly subsonic (Figure 4, bottom left), whereas it is transsonic in most other parts of the envelope and supersonic behind shocks in the outer regions. The envelope is still mostly co-rotating, as can be seen in the angular component of the velocity (Figure 4, bottom middle), although the velocity is rather small in the region of the instability. Especially in the inner part, adjacent layers can be found with differing velocities, resulting in shear flows.

The development of large-scale flow instabilities and an inverse entropy gradient indicate the onset of turbulent convection in the differentially rotating envelope. This supports the assumptions of Meyer & Meyer-Hofmeister (1979) of a co-rotating interior and a differentially rotating envelope with angular momentum transport mediated by convection in the envelope.

Large-scale flow instabilities have not been observed in hydrodynamics simulations before. Passy et al. (2012) show a density distribution for their 256^3 grid run after about five orbits, where only spiral shocks with smooth regions in between are visible (see their Figure 6). The density slice of the AMR simulations by Ricker & Taam (2012) after roughly five orbits displays features that may be caused by shear flows between adjacent spiral shocks. Their simulation was stopped at this instant and it is unclear if large-scale instabilities would have emerged in the further evolution of the model. We suspect, however, that the development of shear instabilities is not seen due to large numerical diffusion in the SPH simulations and due to the background velocity field in the grid simulations. The violation of Galilean invariance in conventional grid-based hydrodynamics codes (when altering the background velocity at the same resolution) suppresses Kelvin–Helmholtz instabilities on a static mesh; this is illustrated in Figure 33 of Springel (2010). The numerical scheme of AREPO is Galilean invariant, thus, shear instabilities may also develop on top of background velocities.

4. CONCLUSIONS

In this Letter, we explore the hydrodynamics of the rapid spiral-in during a CE event using the moving-mesh code AREPO. The combination of the nearly Lagrangian mesh motion and the Galilean-invariant scheme enables us to resolve the hydrodynamical structure in unprecedented detail, and complements recent hydrodynamics simulations (Passy et al. 2012; Ricker & Taam 2012). In particular, we observe, for the first time, the emergence of large-scale flow instabilities. These are caused by shear between adjacent layers of the shock spiral that is created by the in-fall of the companion. These instabilities indicate the onset of turbulent convection, with important consequences for the further evolution of the system by, e.g., altering the energy transport on thermal timescales.

In terms of global quantities, we confirm earlier simulations (Ricker & Taam 2008, 2012; Passy et al. 2012): only a small fraction of the envelope mass is ejected on a dynamical timescale and the final separation is larger than observed. This may be due to the envelope ejection proceeding on a much longer timescale than that followed in our simulation. It is also possible that we miss other processes driving the loss of the envelope, such as recombination.

As a next step, we will improve the modeling of additional microphysical effects, including recombination, and examine different parameters (orbital parameters, masses) to link the final system characteristics to them in a systematic way. This opens up the exciting prospect to directly connect the hydrodynamics simulations to binary stellar evolution.

We thank Jean-Claude Passy, Orsola de Marco, and Philipp Edelmann for helpful discussions. S.T.O. acknowledges support from the Studienstiftung des deutschen Volkes. F.K.R. acknowledges support by the DAAD/Go8 German-Australian exchange program, and by the ARCHES prize of the German Ministry of Education and Research (BMBF). R.P. and V.S. acknowledge support by the European Research Council under ERC-StG grant EXAGAL-308037 and by the Klaus Tschira Foundation. This work was also supported by the graduate school "Theoretical Astrophysics and Particle Physics" at the University of Würzburg (GRK 1147). For data processing and plotting, we used NumPy and SciPy (Oliphant 2007), IPython (Pérez & Granger 2007), and Matplotlib (Hunter 2007).

REFERENCES

Gianninas, A., Dufour, P., Kilic, M., et al. 2014, ApJ, 794, 35
Górski, K. M., Hivon, E., Banday, A. J., et al. 2005, ApJ, 622, 759
Hunter, J. D. 2007, CSE, 9, 90
Ivanova, N., Justham, S., Chen, X., et al. 2013, A&ARv, 21, 59
Kippenhahn, R., Weigert, A., & Weiss, A. 2013, Stellar Structure and Evolution (Berlin: Springer)
Marinacci, F., Pakmor, R., & Springel, V. 2014, MNRAS, 437, 1750
Meng, X. C., Chen, W. C., Yang, W. M., & Li, Z. M. 2011, A&A, 525, A129
Meyer, F., & Meyer-Hofmeister, E. 1979, A&A, 78, 167
Nandez, J. L. A., Ivanova, N., & Lombardi, J. C., Jr 2015, MNRAS, 450, L39
Oliphant, T. E. 2007, CSE, 9, 10
Paczynski, B. 1976, in IAU Symp. 73, Structure and Evolution of Close Binary Systems, ed. P. Eggleton, S. Mitton, & J. Whelan (Dordrecht: Reidel), 75
Pakmor, R., Springel, V., Bauer, A., et al. 2016, MNRAS, 455, 1134
Passy, J.-C., De Marco, O., Fryer, C. L., et al. 2012, ApJ, 744, 52
Paxton, B., Bildsten, L., Dotter, A., et al. 2011, ApJS, 192, 3
Paxton, B., Cantiello, M., Arras, P., et al. 2013, ApJS, 208, 4
Pérez, F., & Granger, B. E. 2007, CSE, 9, 21
Ricker, P. M., & Taam, R. E. 2008, ApJL, 672, L41
Ricker, P. M., & Taam, R. E. 2012, ApJ, 746, 74
Springel, V. 2010, MNRAS, 401, 791
Vogelsberger, M., Genel, S., Springel, V., et al. 2014, Natur, 509, 177